RESEARCH ARTICLE

Check for updates

Phthalocyanine-induced iron active species in metal−organic framework-derived porous carbon for efficient alkaline zinc−air batteries†

Cheng Han,[a] Xiaodeng Zhang,[a] Qiuhong Sun,[a] Dandan Chen,[a] Tingting Miao, [ID][a] Kongzhao Su, [ID][b] Qipeng Li, [ID][b,c] Shaoming Huang [ID][d] and Jinjie Qian [ID]*[a,b]

The oxygen reduction reaction (ORR) on the cathode is of great significance in fuel cells and metal−O_2 batteries, which is well demonstrated and highly efficient in nature. Herein, iron phthalocyanine (FePc) is encapsulated into the nanosized pores of a new porous metal−organic framework (MOF) of **BMM-14** to give **FePc@BMM-14**. It shows a series of atomically dispersed Fe-based active species embedded into N-doped **Fe@NC(x+y)** samples after calcination, where *x* and *y* represent the FePc concentration and temperature, respectively. During pyrolysis, the rapid volatilization of Zn contents can further expand the framework to form more loose carbon nanomaterials with abundant active components, including FeN_x and ultrafine Fe-based nanoparticles. Compared to the state-of-the-art Pt/C, the obtained **Fe@NC (10+900/1000)** exhibits satisfactory ORR performance to give a large limiting current of −5.22/−5.16 mA cm^{-2} (0.3 V *vs.* RHE), small Tafel slope of −51.1/−38.9 mV dec^{-1}, and excellent stability. Meanwhile, the assembled batteries based on the two above catalysts show high activity, indicative of being potential substitutes to those noble metals consolidated by the theoretical calculations. This work demonstrates phthalocyanine-induced Fe-based active species in MOF-derived graphitic carbon as efficient ORR electrocatalysts for zinc−air batteries, which can be extended into the reasonable design and preparation of cost-effective but highly efficient catalysts for various energy-related applications.

1. Introduction

Green renewable energy stands in contrast to fossil fuels and is currently attracting more attention. Globally speaking, the rapid and extensive deployment of renewable energy will result in significant energy security and economic benefits, which in turn can alleviate environmental pollution, improve public health, and reduce associated costs to a large extent.[1–5] Under these circumstances, the key to the large-scale applications of various new clean energy technologies, including renewable fuel cells and secondary batteries, mainly lies in the exploitation of high-efficiency catalysts for oxygen reduction reactions (ORR) on the cathode.[6–11] Although platinum-related nanomaterials have long been recognized as the best catalysts, their low durability and high price severely hinder their further development and wide commercialization.[12,13] Therefore, the development of cheap, robust and high-performance non-noble metal-based substitutes has become one of the research hotspots in the scientific community.

Microporous metal–organic frameworks (MOFs) have been fully demonstrated in gas storage and separation, drug delivery and release, heterogeneous catalysis, and so on.[14–19] As one subclass of crystalline MOFs, zeolite imidazole frameworks (ZIFs) have also been widely investigated on account of their high porosity, adjustable structure, and rich carbon and nitrogen sources.[20,21] MOF materials are structurally rich in inorganic metal units and have a high content of organic ligands that make them potential precursors for multifunctional metal carbon composites. Due to the fast volatilization of Zn species, the formation of porous N-containing carbons calcined from Zn-based ZIFs can be achieved with a great possibility.[22,23] Therefore, a large number of ZIF-derived carbon nanomaterials such as carbon nanotubes and carbon nanosheets have been widely utilized in different energy-related applications, because of their large specific surface area, excellent

[a] Key Laboratory of Carbon Materials of Zhejiang Province, College of Chemistry and Materials Engineering, Wenzhou University, Wenzhou, Zhejiang, P. R. China. E-mail: jinjieqian@wzu.edu.cn
[b] State Key Laboratory of Structural Chemistry, Fujian Institute of Research on the Structure of Matter, Chinese Academy of Sciences, Fuzhou, Fujian, P. R. China
[c] College of Chemistry and Chemical Engineering, Zhaotong University, Zhaotong, Yunnan, P. R. China
[d] School of Materials and Energy, Guangzhou Key Laboratory of Low-Dimensional Materials and Energy Storage Devices, Guangdong University of Technology, Guangzhou, P. R. China

This journal is © the Partner Organisations 2022

Inorg. Chem. Front., 2022, **9**, 2557–2567 | **2557**

electrical conductivity, high stability and other significant advantages.[24–27] In this context, the rational design and facile preparation of porous MOF-derived carbon-based catalysts in energy conversion and storage is highly important and desired.

On the other hand, the phthalocyanine compounds show a large conjugated system of 18 electrons structurally similar to the porphyrins that exist widely in nature.[28,29] Among them, the structure of iron phthalocyanine (FePc) resembles the core of hemoglobin, which is highly selective for adsorption and transport of oxygen in human blood.[30–32] In addition, the atomically dispersive iron active centers have been considered to be an efficient ORR catalyst in those recent reports.[33–35] For example, Dai et al. have synthesized FeN_x species well confined within micropores of the hierarchically porous carbon by the direct pyrolysis of the FePc complex, which outperforms the commercial Pt/C in terms of ORR activity.[36] Meanwhile, these carbon-coated iron nanoparticles (NPs) as active catalytic species could be another type of non-precious metal oxygen reduction catalysts previously demonstrated by the Gewirth group.[37] Thus, the rational combination between MOF and FePc will lead to the formation of Fe-based species after calcination, namely FeN_x sites as well as Fe NPs, which deserves an in-depth investigation for efficient ORR performance.

Herein, a new porous Zn-based MOF (**BMM-14**) is solvothermally synthesized by three different imidazole ligands; for a more detailed experimental procedure please see the ESI.† Through a simple two-solvent diffusion method, discrete FePc can be successfully dispersed into this MOF to yield **FePc@BMM-14(x)**, where x (0.1, 1, 10 g L^{-1}) represents the concentration of FePc within 50 mg of the MOF precursor. After being pyrolyzed at different temperatures, the morphology of **FePc@BMM-14(10)** exhibits a flake-like shape to prove the influence of the introduced phthalocyanine on the obtained carbon. It also shows that the volatilization of Zn species can further expand the carbon layer, which is beneficial for the formation of a more loose N-containing framework, especially for **Fe@NC(10+900/1000)**. These as-calcined Fe,N-doped carbon nanomaterials are endowed with the advantages of high porosity and a large specific surface area, while the low content of FePc results in generating atomically dispersive FeN_x centers and ultrafine Fe nanoclusters. In this case, the optimal products of **Fe@NC(10+900/1000)** present a satisfactory ORR activity, showing the limit current of −5.22/−5.16 mA cm^{-2} at 0.3 V vs. RHE, low Tafel slope of −51.1/−38.9 mV dec^{-1}, and excellent stability compared to the state-of-the-art Pt/C. Meanwhile, the assembled zinc–air batteries (ZABs) based on the Fe@NC catalysts give a superior performance with robust long-term stability, indicative of the potential substitutes to those noble metal based catalysts that are further supported by the following theoretical models. The present work confirms the reasonable design and synthesis of transition metal based ORR electrocatalysts by low-concentration filling of phthalocyanine compounds, which would pave a new pathway to prepare novel catalysts for efficient energy storage and conversion.

2. Experiment

2.1 Reagents and materials

All chemicals and solvents were used in this work without further purification; imidazole (Im, 97%, JNHH), 2-nitroimidazole (nIm, 97%, JNHH), benzimidazole (bIm, 97%, JNHH), zinc nitrate (Zn(NO$_3$)$_2$·3H$_2$O, AR, 99%, Aladdin), iron phthalocyanine (FePc, AR, ≥98%, Aladdin), deionized water (DI H$_2$O, 18 MΩ), N,N-dimethylformamide (DMF, ≥99.8%, Aladdin), n-hexane (≥99.8%, Aladdin), dimethyl sulfoxide (DMSO, ≥99.8%, Aladdin), ethanol (EtOH, >99%, GC, Aladdin), and Nafion ionomer (5 wt%, DuPont).

2.2 Synthesis of Fe@BMM-14(x)

30 mg of **BMM-14** was dispersed in 4 ml of n-hexane, ultrasonicated for 0.5 h and stirred for 1 h. Different concentrations of FePc were dissolved in 1 ml of DMSO solution, then added into n-hexane solution of **BMM-14**, stirred for 1 h, centrifuged and washed with EtOH three times, and dried overnight at 85 °C. The yield of **BMM-14** is calculated to be ~60% based on the added organic ligands.

2.3 Synthesis of Fe@NC(x+y)

The **Fe@NC(x+y)** is synthesized by direct pyrolysis of the as-prepared **Fe@BMM-14(x)** in an Ar atmosphere. The furnace temperature is increased from room temperature at a heating rate of 10 °C min^{-1} to 700/800/900/1000 °C. After maintaining at the target temperature for 1 h, the obtained **Fe@NC(x+y)** is naturally cooled to room temperature. It can maintain ~30% of its total mass at 700/800 °C and only ~20% at 900/1000 °C.

2.4 Electrochemical characterizations

The electrochemical performance of the samples was conducted in a three-electrode system using the Autolab workstation (Metrohm, Swiss) and/or the CHI760E electrochemical workstation (CH Instruments, Shanghai) for ORR, which comprise a counter electrode (graphite rod), a reference electrode (Ag/AgCl (3 M KCl)) and a working electrode (rotating ring-disk glass-carbon with catalyst, disk diameter is 5.6 mm). The working electrode is prepared by depositing the ink of catalysts. In a typical process to make up the electrode ink, 2.5 mg of **Fe@NC(x+y)** is dissolved in a mixed solvent containing 150 μL of EtOH, 100 μL of deionized water, and 2.5 μL of Nafion (5%) to form a homogeneous catalyst ink by ultrasonicating for 3 h. Then 15 μL of the as-prepared droplet is deposited onto the surface of the GCE electrode and dried at room temperature conditions. Before every test, the electrolyte (0.1 M KOH) is pre-purged with pure O$_2$ for 30 min to make sure it is O$_2$-saturated. Firstly, scanning is performed for 40 cycles of cyclic voltammetry (CV) curves until the signals are stabilized. The linear sweep voltammetry (LSV) is scanning at a potential scan rate of 5 mV s^{-1} at different rotational speeds from 100 to 2500 rpm for ORR. For data analysis, all the potentials are transformed with reference to a standard reversible hydrogen electrode (RHE) according to the following equation: $E_{RHE} = E_{Ag/AgCl} + 0.975$ V in 0.1 M KOH. To evaluate the active

2558 | Inorg. Chem. Front., 2022, **9**, 2557–2567

This journal is © the Partner Organisations 2022

surface area of catalysts, the double-layer capacitance (C_{dl}) is determined by measuring the CV plots from 1.00 to 1.10 V *vs.* RHE at various scan rate from 5 to 25 mV s^{-1} in N$_2$-saturated 0.1 M KOH in the nonfaradaic potential region. By fitting the current density at 1.15 V *vs.* RHE at various scan rates, the linear trend is observed and found equal to the slope of the linear C_{dl}. All electrochemical impedance spectroscopy (EIS) measurements were recorded at the same overpotential of 0.8 V *vs.* RHE in the frequency range of 10^{-2}–10^6 Hz with an amplitude of 5 mV. Electrocatalytic stability was obtained using the current–time (i–t) chronoamperometric curve at 0.6 V in O$_2$-saturated 0.1 M KOH for 10 h.

The electron transfer number (n) and yield of the H$_2$O$_2$ intermediate were calculated according to the Koutecky–Levich (K–L) eqn (1) and (2) and RRDE technologies eqn (3) and (4), as shown below:

$$\frac{1}{j} = \frac{1}{j_L} + \frac{1}{j_K} \tag{1}$$

$$j_L = \frac{0.2nFC_0D_0^{\frac{2}{3}}}{v^{\frac{1}{6}}} \cdot \frac{1}{\omega^{\frac{1}{2}}} = B \cdot \frac{1}{\omega^{\frac{1}{2}}} \tag{2}$$

$$n = \frac{4I_d}{I_d + \dfrac{I_r}{N}} \tag{3}$$

$$H_2O_2\ (\%) = \frac{\dfrac{2I_r}{N}}{|I_d| + \dfrac{I_r}{N}} \times 100\% \tag{4}$$

In these formulae, J is the experimental current density, J_L is the diffusion-limited current density, and J_K is the kinetic current density, respectively; ω is the rotation speed in rpm (round per minute), F is the Faraday constant (96 485 C mol^{-1}), C_0 is the bulk concentration of oxygen (1.2×10^{-6} mol cm^{-3}), D_0 is the diffusion coefficient of oxygen in 0.1 M KOH (1.9×10^{-5} cm^2 s^{-1}), and v is the kinetic viscosity (0.01 cm^2 s^{-1}). When the speed of rotation is also represented as rpm, 0.2 is a constant. The n can be extracted from the slope of the K–L plot. I_r is the ring current, I_d is the disk current and N expresses the collection efficiency of the ring electrode (0.37).

The aforesaid obtained electrocatalyst ink as the cathode is dropped onto carbon paper until the loading mass is 1.0 mg cm^{-2} and dried in air. Besides, one Zn foil becomes the anode and the paper is used to absorb 6.0 M KOH electrolytes and separate the electrodes. Finally, these materials are assembled in perforated button-cell shells for testing. All Zn–air button battery tests are performed under ambient atmosphere at room temperature. Discharge power density is calculated from the discharge polarized profiles using the following equation:

$$P = U_d \times J_d$$

where the P, U_d, and J_d are the discharge power density, discharge voltage, and discharge current density, respectively.

2.5 Theoretical calculation

The constructed models of FeN$_x$ composites are optimized by the CASTEP module of the Materials Studio 8.0 software to obtain the geometry optimized structure with minimized energy, in which the functional is chosen as the Perdew–Burke–Ernzerhof (PBE) functional in generalized gradient approximation (GGA). The basic model contains four benzene rings; one of the benzene rings is removed, and Fe atoms are introduced to construct these target FeC$_x$N$_y$ sites. In this computation, the graphene surface is modeled in a 2×2 supercell; the cell size is $a = b = 9.839996$, $c = 6.8$; $\alpha = \beta = 90°$, $\gamma = 120°$, with one Fe atom doped layer and a vacuum layer of 8 Å. The Brillouin zone is sampled with $3 \times 4 \times 1$ k-points and cut-off energy of 300 eV is used. And PDOS analysis was added in the calculation process. The adsorption energy (E_a) of O$_2$ with FeN$_x$ is calculated by the following equation, where E_{O_2+sub}, E_{O_2}, and E_{sub} are the energy of the FeN$_x$ substance combined with the oxygen, oxygen molecule, and FeN$_x$ substance, respectively.

$$E_a = E_{O_2+sub} - E_{O_2} - E_{sub}$$

3.   Results and discussion

The self-assembly of imidazole (Im), nitroimidazole (nIm) and benzimidazole (bIm) together with Zn(II) cations leads to the formation of orange crystals (Fig. 1a). Meanwhile, the optical microscope and scanning electron microscope (SEM) images show that the obtained **BMM-14** exhibits a prism connected to two hexagonal pyramids. Its cell unit and asymmetric unit (AU) of the single-crystal structure are depicted in Fig. 1c and S1,† respectively. As a result of various imidazole linkers, there are three different secondary building units (SBUs), namely SBU-1 (Im + 2bIm + nIm, red circle), SBU-2 (2Im + bIm + nIm, yellow circle) and SBU-3 (Im + bIm + nIm + NO$_3^-$, green circle) in Fig. 1b. In this case, the metal sites in each SBU adopt the typical ZnN$_4$ consistent with the previously reported examples of Zn-imidazole MOFs.[38] Finally, 1-dimensional tubular nano-channels are formed along the c-axis; for more information on the structure please refer to Fig. S2 and Table S1.† The bIm along the ab plane obstructs the largest channel of 20.1 Å to a small gap of around 11.9 Å, which can completely encapsulate FePc (13.1 Å) in Fig. 1c and d. The black dotted area in Fig. 1c is the largest cavity in **BMM-14** that is simply selected to demonstrate the schematic diagram of FePc molecular packing (Fig. 1e). It shows that there is enough space between the two layers of Zn atoms to fill FePc, and will not be disturbed by bIm (Fig. S3†). Furthermore, the thermogravimetric analysis (TGA) under N$_2$ flow in Fig. S4† reveals the structural change of **BMM-14** in the heating process where the first weight loss is ascribed to the dehydration of physically adsorbed solvents before 320 °C, while the second loss belongs to the removal of the coordinating small molecules in 320–500 °C. The final sharp weight loss corresponds to a gradual decomposition of organic ligands into porous carbon materials.

This journal is © the Partner Organisations 2022

Inorg. Chem. Front., 2022, **9**, 2557–2567 | **2559**
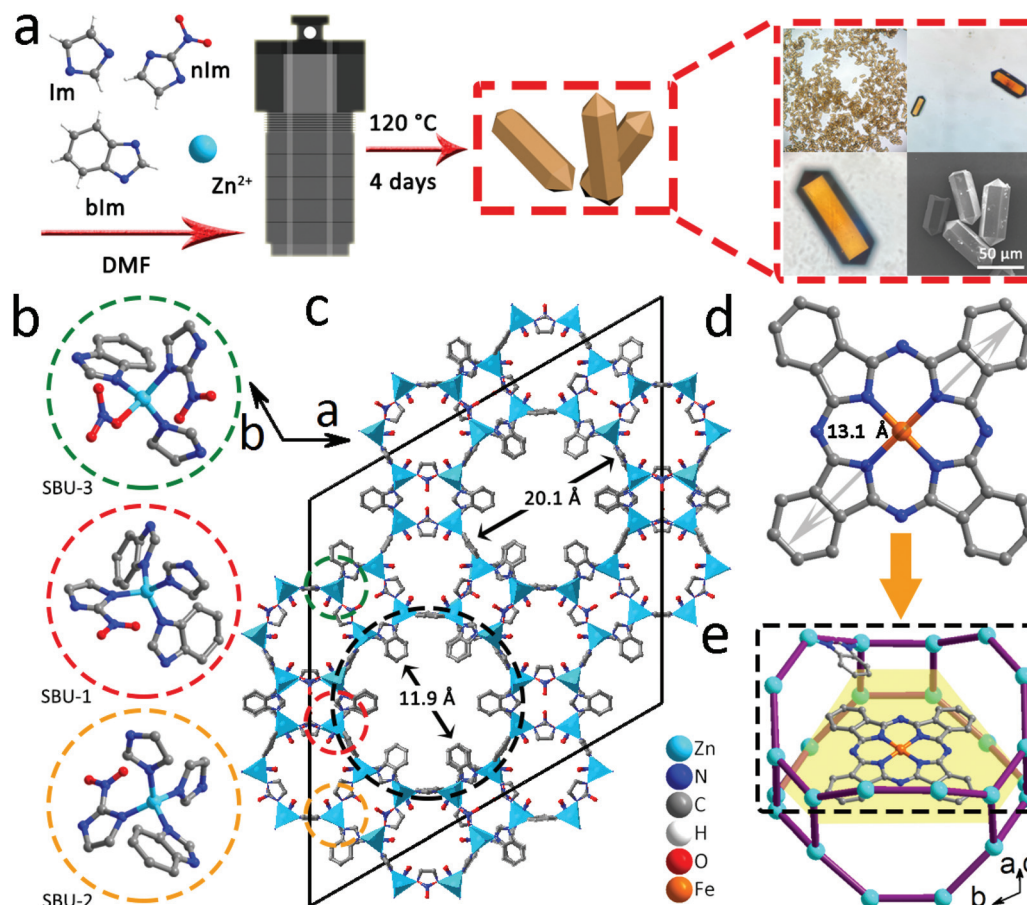
Fig. 1 (a) The route to prepare **BMM-14** single crystals and their optical/SEM images; (b) three different Zn–based SBUs; (c) the cell unit; (d and e) FePc molecule and its encapsulation in a MOF cavity.

Due to the large porosity and abundant channels, a simple double-solvent dispersion method is used to encapsulate different amounts of FePc molecules.[39] In Fig. 2a, the powder X-ray diffraction (PXRD) verifies that the as-made **BMM-14** crystals are in good agreement with the simulated peaks, in which four strong diffraction signals at 2-theta values of 6.2°, 6.7°, 9.7°, and 10.2° are well matched with the (2, −1, 1), (3, 0, 0) (0, 2, 2) and (2, −1, 2) planes, respectively. After that, a total of 50 mg of pristine MOF is dispersed in 4 mL of n-hexane, while x (0.1, 1, 10) g L^{-1} of FePc in dimethyl sulfoxide is also prepared, then the above two solvents are mixed to obtain the **FePc@BMM-14(x)** sample. From FT-IR spectra, there are no new characteristic peaks detected after loading with different concentrations of FePc into the crystalline MOF (Fig. 2b). However, the optical color of the exchanged samples exhibits a significant change confirmed by the UV-vis spectra before and after the dispersion treatment in Fig. 2c and S5.† The PXRD patterns of FePc-encapsulated MOFs show that the obtained **FePc@BMM-14(10)** with the highest concentration owns a typical characteristic peak at 27.1° validating the successful loading of FePc (Fig. 2d). Meanwhile, the composite presents no obvious difference in the crystal form, of which the overall framework is almost retained. In Fig. 2e and f, these collected

N_2 isotherms exhibit the type-I curves, and a trend of reduced gas capacity with the filling of FePc is also observed. Furthermore, the fitted pore size distribution (PSD) curves can further confirm that all the pores and channels are centered in the microporous regions, while the number of micropores of **FePc@BMM-14(x)** is significantly reduced after the loading of FePc. For more specific surface area and PSD data please see Table S2.† It is indicative that the small FePc molecule has been evenly distributed in the MOF cavity that will be conducive to the formation of dispersive Fe atoms after the subsequent thermal treatment.

The morphology change of the **FePc@BMM-14** series is first studied by SEM images. After continuous stirring, the bulk single crystals are cracked into micro-sized particles with an increased FePc concentration to achieve an adequate dispersion. For the control sample of **FePc@BMM-14(0)**, there is no difference compared with the broken particles in Fig. 3a1, a2 and S6.† However, the surface of **FePc@BMM-14(x)** becomes significantly rough (Fig. 3b–d and S7–S9†), especially for **FePc@BMM-14(10)**, which is reasonably selected to carry out the following thermal treatments. After calcination, these original particles will be almost destroyed which can be reflected in the products of **Fe@NC(10+900/1000)** with the
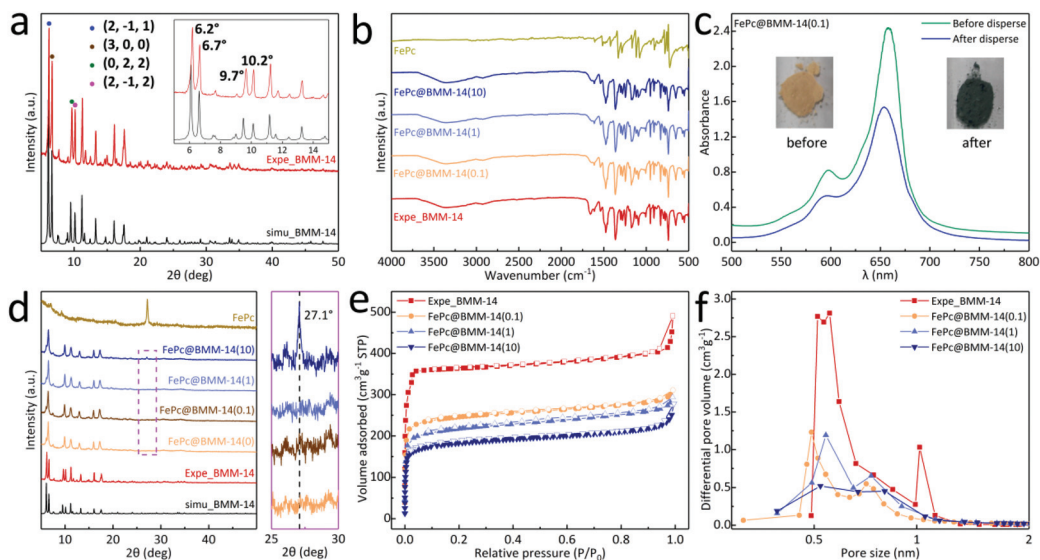
Fig. 2 (a) PXRD patterns; (b) FT-IR spectra of **FePc@BMM-14** series and FePc; (c) UV-vis curves before and after dispersing FePc; (d) PXRD patterns, (e) N$_2$ isotherms at 77 K and (f) PSD curves of **FePc@BMM-14(x)** samples.

most obvious sheet-like structure. This can be well explained by the bubbling process induced by the volatilization of Zn species in the carbon layer, thereby achieving the pore-forming effect.[40] The subsequent gas sorption and PSD data verify that the obtained **Fe@NC(10+900/1000)** possess a higher adsorption capacity with distinct hysteresis loops in Fig. 3g, h, S13 and S14.† However, the total N$_2$ uptake of **Fe@NC(10+700/800)** does not change significantly, which stemmed from the lower carbonization process in Fig. 3e, f, S11 and S12.† Meanwhile, the increased BET surface areas are in the following order **Fe@NC(10+700)** (60.32 m^2 g^{-1}), **Fe@NC(10+800)** (104.00 m^2 g^{-1}), **Fe@NC(10+900)** (334.75 m^2 g^{-1}), and **Fe@NC(10+1000)** (420.30 m^2 g^{-1}), respectively. Furthermore, the difference in PSD further proves that the carbon at higher temperature presents the larger total pore volume induced by the Zn evaporation. The enhanced micropore content of **Fe@NC(10+900/1000)** is indicative of the superiority of both carbon nanomaterials which are endowed with abundant active sites that would accelerate the electron transfer and mass diffusion during the electrochemical performance.

Transmission electron microscopy (TEM) and high resolution TEM (HR-TEM) further reveal the nanostructure and morphological features of these carbon materials. In Fig. 4a1–d1, the **Fe@NC(10+y)** series present the microstructure of bulky body and sheet-shaped edge, but the nanosheet structures of **Fe@NC(10+700/800)** are not as obvious as **Fe@NC(10+900/1000)**, which verifies the incompleteness of low-temperature carbonization and the characteristics of amorphous carbon. Each sample shows the tendency of the carbon layer to wrap the metal sources where the distribution of metals is relatively compact and poorly dispersive, especially for **Fe@NC(10+700/800)** (Fig. 4a2–d2). In this case, the metal aggregation in the graphitic carbon comes from a large amount of Zn from the MOF precursor as well as Fe from the FePc molecules. On the

other hand, the ultrafine NPs are evenly distributed and atomically dispersive metals wrapped in the N-doped carbons are detected in **Fe@NC(10+900/1000)**. Meanwhile, low-temperature carbonization leads to the formation of some inconspicuous lattice stripes of carbon (0.33 nm) in Fig. 4a3 and b3. An ordered nanostructure on the edge corresponds to the (0 0 2) plane of graphite for **Fe@NC(10+800)** confirming the existence of graphitized carbon, but the inner carbon maintains a disordered structure (Fig. 4b3). However, the inner/outer carbon reaches an ordered structure for **Fe@NC(10+900)** in Fig. 4c2 and c3, and a small number of cavities are *in situ* formed during pyrolysis. The same phenomenon can also be detected in **Fe@NC(10+1000)** where cavities in the middle of the carbon layer become more obvious. Meanwhile, the hollow carbon structure coated with Fe atoms shows orderly structure characteristics in Fig. 4d2 and d3, and for more TEM images please refer to Fig. S15–S18.† Finally, the uniform distribution of **Fe@NC(x+y)** can be clearly examined in the EDX spectra and elemental mappings (Fig. 4a4–d4). This is indicative of the successful formation of the thermodynamically stable FeN$_x$ species because of the low content of FePc in the microporous channels. The obtained hierarchically porous and graphitic carbon nanomaterials ensure the fast transfer of the electrolytes and electrons, and the active sites are thoroughly exposed to achieve the enhanced electrochemical performance under an extremely high atomic utilization.

To characterize the content and coordination environment, X-ray photoelectron spectroscopy (XPS) is performed to show the coexistence of Zn, Fe, C, N, and O (Fig. 5a and S19†). Almost invisible Fe 2p peaks in the full spectra of **Fe@NC(10+900/1000)** confirm the presence of trace FePc introduced in the MOF pores. Meanwhile, the decrease or even disappearance of the Zn 2p signal also proves the evaporation of Zn after high temperature carbonization.[41] In Fig. 5b, S20 and
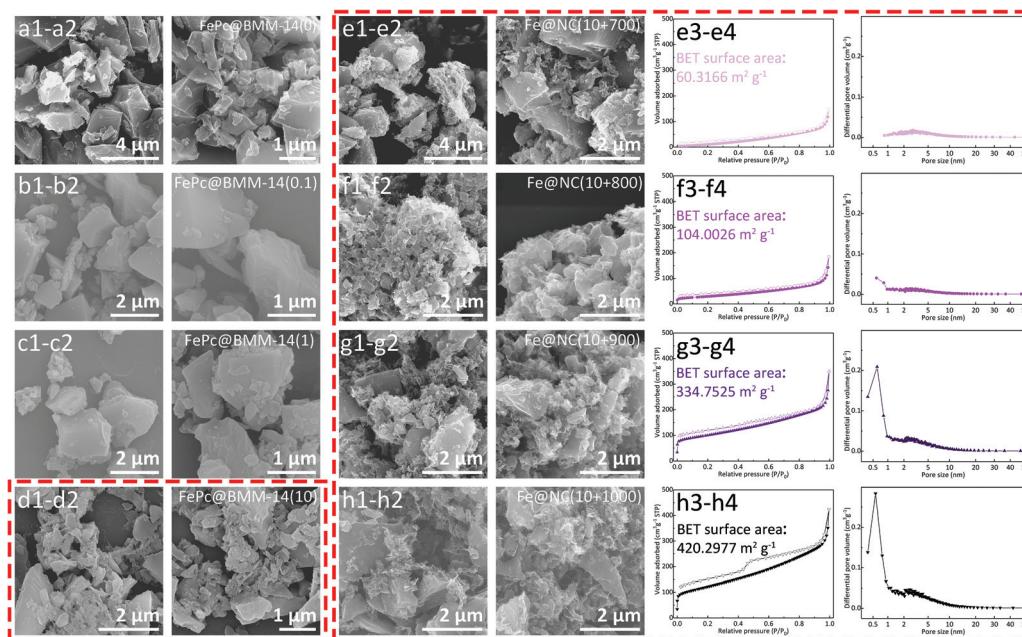
This journal is © the Partner Organisations 2022

Inorg. Chem. Front., 2022, **9**, 2557–2567 | **2561**

Fig. 3 SEM images of (a–d) **FePc@BMM-14(x)**; (e–h) SEM images, sorption isotherms and PSD curves for the calcined **Fe@NC(10+y)** series.

Table S3,† the deconvoluted O 1s peak shapes in **Fe@NC(0/10+900)** are almost the same where three peaks at 530.1, 531.2 and 532.2 eV are considered as the M–O, C–O and the C═O bonds, respectively. The deconvoluted C 1s spectra in Fig. 5c reveal the existence of four different carbon coordination environments (C–C sp^3, C═C sp^2, C–O/C–N and C═O/C═N) and there is no change in the positions of the four peaks, which confirms that the coordination environment of carbon atoms in the five material has not changed during the change of pyrolysis temperature. In this case, element N mainly comes from imidazoles in the microporous MOF in the high-resolution spectra of N 1s in Fig. 5d and Table S5.† The fitting peak positions of N in **Fe@NC(10+900/1000)** exhibit almost no deviations, indicating that the high-temperature carbonization poses no influence on the coordination environment of Fe and N. On the other hand, the changes in the coordination environment of Zn and Fe have been further studied in Fig. 5e and f. There is a slight negative shift trend of the 2p$_{1/2}$ and 2p$_{3/2}$ peak positions of Zn(II) in **Fe@NC(10+700/800)** compared to those in **Fe@NC(10+900/1000)**, while the binding energies of 2p$_{1/2}$ and 2p$_{3/2}$ of Fe(0, II, III) tend to shift in the positive direction compared to those of **Fe@NC(10+900/1000)**. The deconvoluted Fe 2p spectra show three pairs of weak peaks at 706/720, 709/721, and 712/724 eV for Fe(0), Fe(II), and Fe(III), respectively, implying the Fe–N$_x$ sites in **Fe@NC(10+y)** samples. At higher temperatures, the binding energies of 2p$_{1/2}$ and 2p$_{3/2}$ of Zn(II) for **Fe@NC(10+900/1000)** suddenly rise as a result of the reduction and evaporation of Zn(II) species, while the binding energies of 2p$_{1/2}$ and 2p$_{3/2}$ of Fe(0, II, III) decrease, especially in Fe(II) and Fe(0). For more XPS data and peak changes, please refer to Fig. S19–S22 and Tables S3–S7.†

Inspired by the nanostructure as well as abundant FeN$_x$ species in **Fe@NC(x+y)**, the electrochemical ORR performance is further evaluated in 0.1 M KOH, and all applied potentials have been calibrated to the reversible hydrogen electrode. In Fig. 6a, the cyclic voltammetry (CV) curves in N$_2$-/O$_2$-saturated solution at 5 mV s^{-1} show that the obtained **Fe@NC(0+900)** owns the inferior oxygen reduction peak of 0.798 V. It reveals that the position of the reduction peak has moved significantly to 0.854/0.912/0.915/0.921 V for **Fe@NC(10+700/800/900/1000)**, respectively, but it is still lower than Pt/C (0.940 V). Meanwhile, the linear sweep voltammograms (LSV) at 1600 rpm in Fig. 6b for **Fe@NC(10+900/1000)** exhibit a higher onset potential and a larger diffusion limited current density (J_L) of −5.22/−5.16 mV cm^{-2} at 0.3 V, higher than **Fe@NC(0+900)** (−2.49 mV cm^{-2}), **Fe@NC(10+700/800)** (−3.99/−4.24 mV cm^{-2}), and Pt/C (−4.95 mV cm^{-2}). When compared to previous reports, the **Fe@NC(10+900/1000)** catalyst demonstrates a competitive ORR performance in Table S8.† The LSV curves from 100 to 2500 rpm are summarized, and the Koutecky–Levich curves of **Fe@NC(10+900/1000)** present almost linear and parallel fitting lines from 0.3–0.7 V (Fig. S23 and S24†). In Fig. 6c, all samples possess relatively small Tafel slopes for **Fe@NC(10+700/800/900/1000)** (−48.6/−47.4/−51.1/−38.9 mV dec^{-1}) lower than Pt/C (−54.2 mV dec^{-1}), indicating the excellent reaction kinetics with enhanced mass transfer ability. Furthermore, the calculated number of transferred electrons (n) and the HO$_2^-$ yields validate the high O$_2$ selectivity and effective 4-electron process (Fig. 6d). The electrochemical impedance spectrum (EIS) in Fig. 6e shows that the obtained **Fe@NC(10+1000)** is endowed with the low charge transfer resistance of 7.2 Ω in the high-frequency region, lower than for **Fe@NC(0+900)** (9.4 Ω), **Fe@NC(10+700/800/900)** (14.5/7.6/12.0
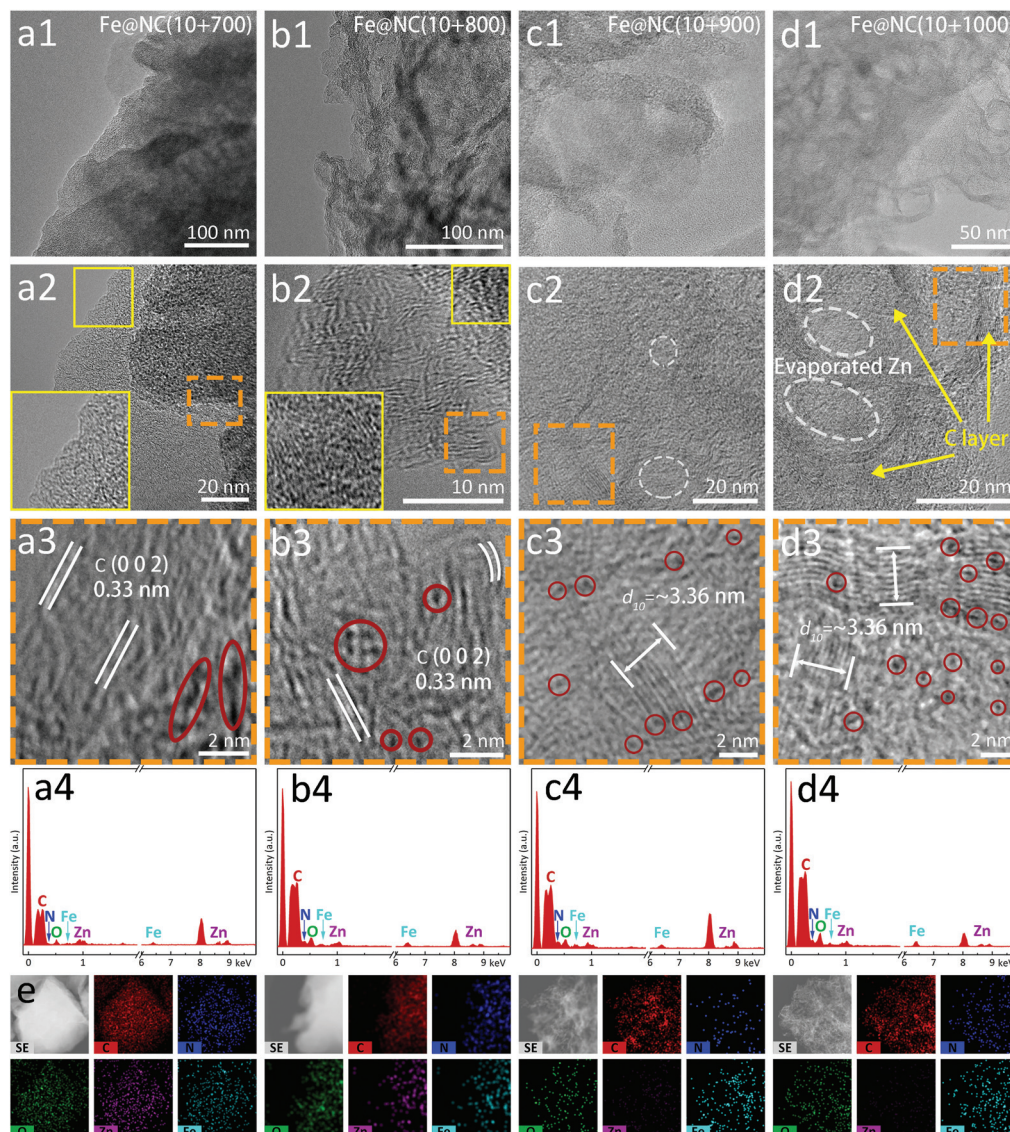
2562 | *Inorg. Chem. Front.*, 2022, **9**, 2557–2567

This journal is © the Partner Organisations 2022

Fig. 4 TEM/HR-TEM images, EDX spectra of (a1–a4) **Fe@NC(10+700)**, (b1–b4) **Fe@NC(10+800)**, (c1–c4) **Fe@NC(10+900)** and (d1–d4) **Fe@NC(10+1000)**. (e) Elemental mappings of **Fe@NC(10+1000)**.
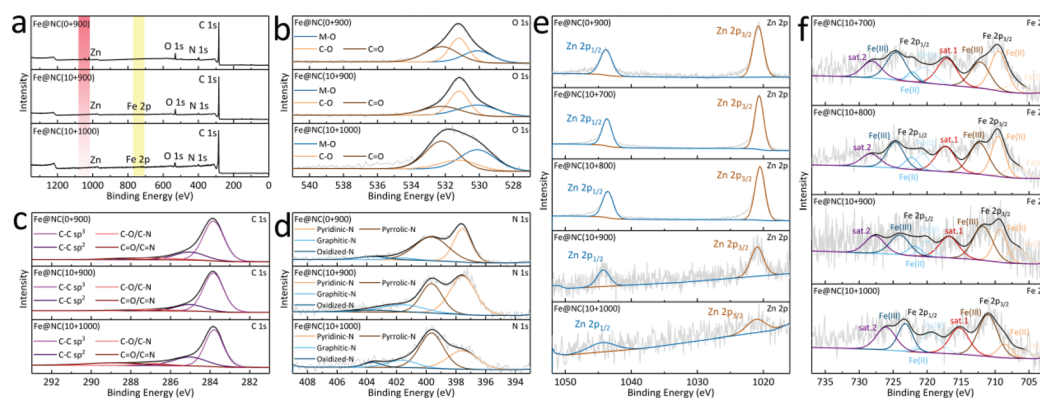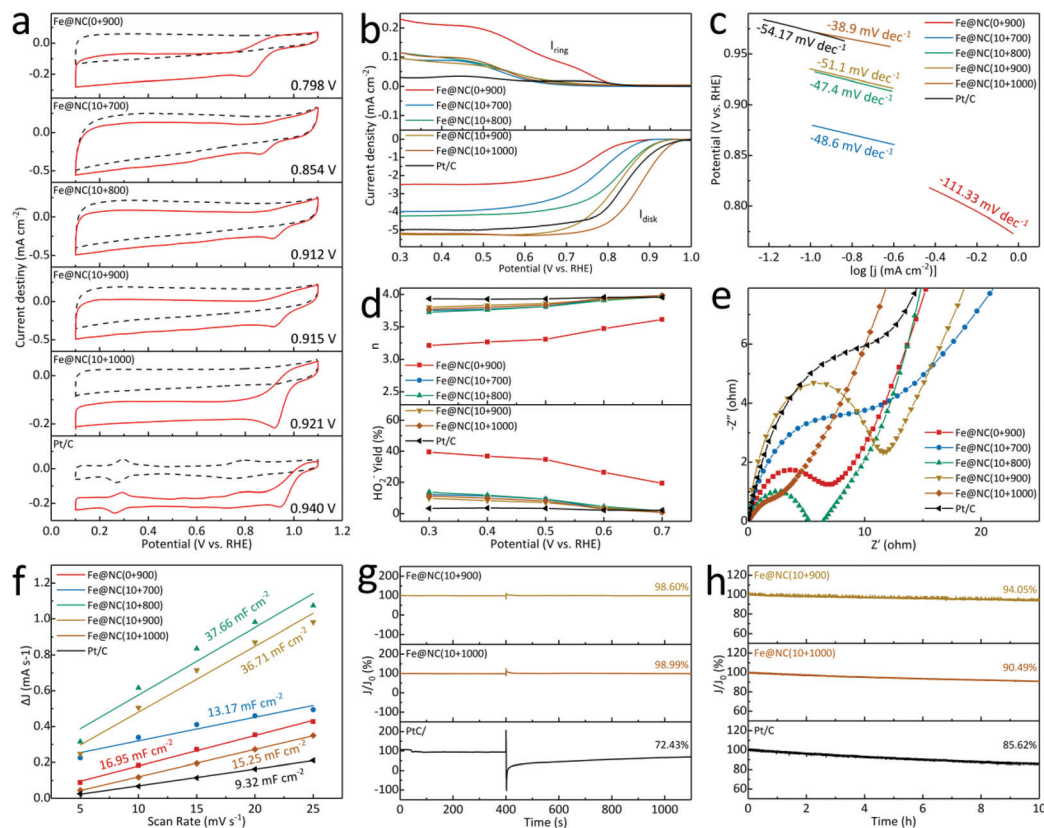

Fig. 5 (a) Full XPS survey spectra; the deconvoluted (b) O 1s, (c) C 1s and (d) N 1s of **Fe@NC(0+900)** and **Fe@NC(10+900/1000)**; the deconvoluted (e) Zn 2p and (f) Fe 2p of **Fe@NC(0+900)** and **Fe@NC(10+y)**.
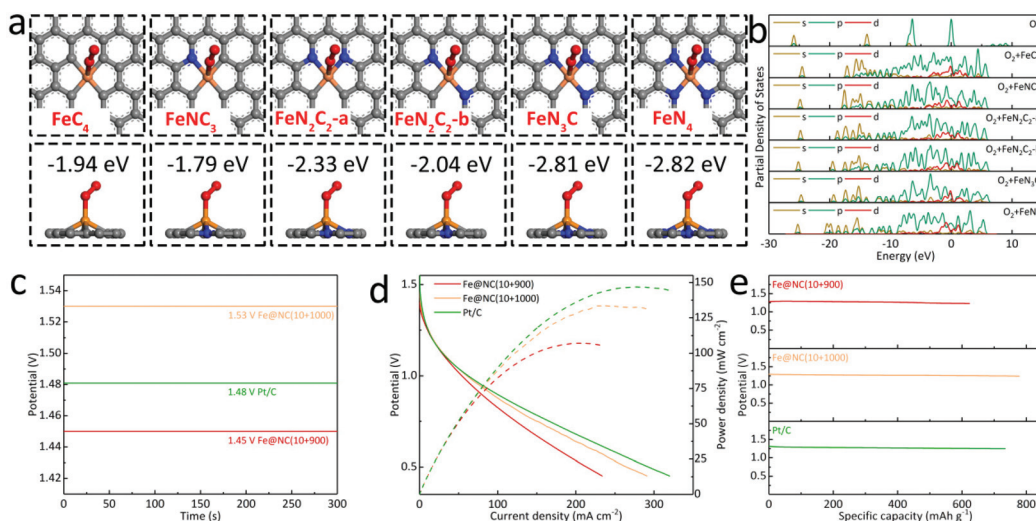
Fig. 6 (a) CV curves, (b) LSV curves, (c) Tafel slopes, (d) n and HO_2^- yields, (e) EIS plots, (f) C_{dl} values for **Fe@NC(x+y)** series and Pt/C; (g) anti-MeOH test, and (h) current retention for **Fe@NC(10+900/1000)** and Pt/C.

Ω) and Pt/C (18.8 Ω). On the other hand, the calculated double-layer capacitance (C_{dl}) shows that **Fe@NC(10+800/900)** (37.66/36.71 mF cm^{-2}) owns a larger electrochemical surface area than **Fe@NC(10+700/1000)** (13.17/15.25 mF cm^{-2}), **Fe@NC(0+900)** (16.95 mF cm^{-2}) and Pt/C (9.32 mF cm^{-2}), proving that both high temperature and multi-element doping can improve the ability of electron/ion transport (Fig. 6f and S25†). By inserting methanol, the excellent tolerance of **Fe@NC(10+900/1000)** with current retention of 98.60%/98.99% is observed compared to Pt/C of 72.43% with an obvious current attenuation in Fig. 6g. Finally, a constant current at 0.6 V is also performed at a rotation rate of 1600 rpm to evaluate the long-term ability in Fig. 6h. The loss is calculated to be 94.05% for **Fe@NC(10+900)** and 90.49% for **Fe@NC(10+1000)** better than that of 20 wt% Pt/C (85.62%), verifying the robust stability. Above all, these porous carbon nanomaterials not only behave as a rigid supporting substrate to mitigate the structural change of catalysts, but also improve the electrochemical property with well dispersed Fe-based active centers.

In order to better understand the improvement of ORR performance in the **Fe@NC(x+y)** series, the theoretical calculations are used to clarify the adsorption behavior of the oxygen molecule on different types of Fe/N-doped graphitic carbon (FeN$_x$C$_y$). There are a total of six differentiated situations for Fe and N coordination environments, namely FeC$_4$, FeNC$_3$, FeN$_2$C$_2$-a, FeN$_2$C$_2$-b, FeN$_3$C and FeN$_4$. First of all, the

standard model of the O$_2$ unit cell is established, and its calculated energy is about −867.91 eV (Fig. S26†). In Fig. 7a, S27 and S28,† it shows that FeN$_x$C$_y$ sites doped with N have lowered the adsorption energy of O$_2$ loaded on the active sites as FeC$_4$ (−1.94 eV), FeNC$_3$ (−1.79 eV), FeN$_2$C$_2$-a (−2.33 eV), FeN$_2$C$_2$-b (−2.04 eV), FeN$_3$C (−2.81 eV) and FeN$_4$ (−2.82 eV). In this case, FeNC$_3$ exhibits a higher adsorption energy than the pristine FeC$_4$ caused by an inevitable breakdown of structural symmetry.[42] With greater N-doping, the overall adsorption energy can be further reduced with more π electrons, which are experimentally supported by the high-efficiency ORR activity of FeN$_x$ sites in our work. In Fig. 7b, the partial density of states (PDOS) for FeN$_x$C$_y$ at approximately 0, −6.42, and −13.87 eV are significantly broadened by valence hybridization compared to the isolated O$_2$ molecule. Furthermore, FeNC$_3$, FeN$_2$C$_2$-a/b, FeN$_3$C and FeN$_4$ are also endowed with obviously lower energies than that of FeC$_4$, indicating the transfer of the partial charge from oxygen to the metal atom in the N-coordinated centers.[43] In addition, we have further applied the optimal samples to assemble Zn–air batteries (ZABs). In Fig. 7c, the **Fe@NC(10+1000)** provides the largest open circuit voltage (OCV) of 1.53 V, higher than Pt/C (1.47 V) and **Fe@NC (10+900)** (1.45 V). Meanwhile, the maximum current density and peak power density of **Fe@NC(10+900)** in Fig. 7d are calculated to be 233.6 mA cm^{-2} and 107.1 mW cm^{-2}, which is inferior to that of **Fe@NC(10+1000)** (291.0 mA cm^{-2},

2564 | *Inorg. Chem. Front.*, 2022, **9**, 2557–2567

This journal is © the Partner Organisations 2022

Fig. 7 (a) Optimized structures of Fe active centers; (b) PDOS after the adsorption of O_2 for FeN_xC_y; (c) OCV curves, (d) polarization and power density profiles, and (e) galvanostatic discharge curves at 10 mA cm^{-2} for **Fe@NC(10+900/1000)** and Pt/C based ZABs.

133.0 mW cm^{-2}), while the Pt/C based ZAB exhibits the best performance of 319.7 mA cm^{-2} and 146.8 mW cm^{-2}. Furthermore, the specific capacity of the Pt/C-based battery is 734.0 mA h g^{-1}, lower than that of **Fe@NC(10+1000)** at 777.6 mA h g^{-1} (Fig. 7e). These above results confirm the high catalytic ORR performance and high stability in alkaline media for MOF-derived porous carbons with abundant FeN_x sites as well as Fe-based NPs. And the long-term charge and discharge curves of the ZABs with **Fe@NC(10+1000)** and Pt/C show a high round-trip efficiency of 52% and 54% within 100 cycles to confirm their robust stability for possible practical devices (Fig. S29†).

4. Conclusion

All in all, we have successfully obtained one new Zn-based **BMM-14** with three different imidazole linkers and 1-dimensional large pores, which are so large that they can be efficiently filled with discrete FePc complexes without agglomeration and accumulation. By adjusting various carbonization temperatures, the FePc-encapsulating **FePc@BMM-14(x)** can be thermally converted into a series of Fe-based active centers embedded into 2-dimensional N-doped carbon nanomaterials, denoted as **Fe@NC($x+y$)**. In addition, the high-temperature evaporation of Zn species leads to the formation of large voids and abundant active materials (including atomically dispersive FeN_x and ultrafine Fe-based NPs) in the graphitic carbon layer. They are more conducive to the exposure of active centers and fast mass transfer during electrochemical reactions. Therefore, the most optimal catalysts of **Fe@NC(10+900/1000)** are better than the commercial Pt/C in terms of mass activity, long-term durability and methanol tolerance, and are used as cathode materials for efficient alkaline ZABs and further confirmed by the theoretical calculations. This work proposes an effective

method to introduce 0-dimensional transition metal active materials into large size-compatible pores of a N-containing MOF precursor that is further pyrolyzed into highly active and stable metal carbon oxygen reduction electrocatalysis. It will shed light on the rational design and synthesis of cost-effective, high-performance and robust electrocatalysts for energy-related applications in the near future.

Author contributions

The manuscript was written through the contributions of all authors. All authors have given approval to the final version of the manuscript.

Conflicts of interest

There are no conflicts of interest to declare.

Acknowledgements

References

1 S. Chaemchuen, N. A. Kabir, K. Zhou and F. Verpoort, Metal-organic frameworks for upgrading biogas via CO_2

This journal is © the Partner Organisations 2022

Inorg. Chem. Front., 2022, **9**, 2557–2567 | **2565**

adsorption to biogas green energy, *Chem. Soc. Rev.*, 2013, **42**, 9304–9332.

2 K. Hartlieb, J. Holcroft, P. Moghadam, N. Vermeulen, M. Algaradah, M. Nassar, Y. Botros, R. Snurr and J. Stoddart, CD-MOF: A Versatile Separation Medium, *J. Am. Chem. Soc.*, 2016, **138**, 2292–2301.

3 D. Li, M. Kassymova, X. Cai, S.-Q. Zang and H.-L. Jiang, Photocatalytic CO_2 reduction over metal-organic framework-based materials, *Coord. Chem. Rev.*, 2020, **412**, 213262.

4 X. Cui, S. Shyshkanov, T. Nguyen, A. Chidambaram, Z. Fei, K. Stylianou and P. Dyson, CO_2 Methanation via Amino Alcohol Relay Molecules Employing a Ruthenium Nanoparticle/Metal Organic Framework Catalyst, *Angew. Chem., Int. Ed.*, 2020, **59**, 16371–16375.

5 X. Zhang, Y. Zhang, Q. Li, X. Zhou, Q. Li, J. Yi, Y. Liu and J. Zhang, Highly efficient and durable aqueous electrocatalytic reduction of CO_2 to HCOOH with a novel bismuth-MOF: experimental and DFT studies, *J. Mater. Chem. A*, 2020, **8**, 9776–9787.

6 X. F. Lu, B. Y. Xia, S. Q. Zang and X. W. D. Lou, Metal-Organic Frameworks Based Electrocatalysts for the Oxygen Reduction Reaction, *Angew. Chem., Int. Ed.*, 2020, **59**, 4634–4650.

7 Z. Liang, H. Guo, G. Zhou, K. Guo, B. Wang, H. Lei, W. Zhang, H. Zheng, U.-P. Apfel and R. Cao, Metal-Organic-Framework-Supported Molecular Electrocatalysis for the Oxygen Reduction Reaction, *Angew. Chem., Int. Ed.*, 2021, **60**, 8472–8476.

8 L. Yang, X. Zeng, W. Wang and D. Cao, Recent Progress in MOF-Derived, Heteroatom-Doped Porous Carbons as Highly Efficient Electrocatalysts for Oxygen Reduction Reaction in Fuel Cells, *Adv. Funct. Mater.*, 2018, **28**, 1704537.

9 I. T. Kim, S. Shin and M. W. Shin, Development of 3D interconnected carbon materials derived from Zn-MOF-74@carbon nanofiber web as an efficient metal-free electrocatalyst for oxygen reduction, *Carbon*, 2018, **135**, 35–43.

10 H. F. Wang, L. Chen, H. Pang, S. Kaskel and Q. Xu, MOF-derived electrocatalysts for oxygen reduction, oxygen evolution and hydrogen evolution reactions, *Chem. Soc. Rev.*, 2020, **49**, 1414–1448.

11 Y. Wang, J. Wang, D. Wei and M. Li, A "MOF-Protective-Pyrolysis" Strategy for the Preparation of Fe-N-C Catalysts and the Role of Fe, N, and C in the Oxygen Reduction Reaction in Acidic Medium, *ACS Appl. Mater. Interfaces*, 2019, **11**, 35755–35763.

12 L. Zhang, H. Li and J. Zhang, Kinetics of oxygen reduction reaction on three different Pt surfaces of Pt/C catalyst analyzed by rotating ring-disk electrode in acidic solution, *J. Power Sources*, 2014, **255**, 242–250.

13 X. Yan, Y. Jia, L. Zhang and X. Yao, Platinum stabilized by defective activated carbon with excellent oxygen reduction performance in alkaline media, *Chin. J. Catal.*, 2017, **38**, 1011–1020.

14 H. Li, K. Wang, Y. Sun, C. T. Lollar, J. Li and H.-C. Zhou, Recent advances in gas storage and separation using metal-organic frameworks, *Mater. Today*, 2018, **21**, 108–121.

15 B. Li, H. M. Wen, W. Zhou and B. Chen, Porous Metal-Organic Frameworks for Gas Storage and Separation: What, How, and Why?, *J. Phys. Chem. Lett.*, 2014, **5**, 3468–3479.

16 M. Kotzabasaki and G. E. Froudakis, Review of computer simulations on anti-cancer drug delivery in MOFs, *Inorg. Chem. Front.*, 2018, **5**, 1255–1272.

17 Y. Xie, X. Liu, X. Ma, Y. Duan, Y. Yao and Q. Cai, Small Titanium-Based MOFs Prepared with the Introduction of Tetraethyl Orthosilicate and Their Potential for Use in Drug Delivery, *ACS Appl. Mater. Interfaces*, 2018, **10**, 13325–13332.

18 L. Ma, C. Abney and W. Lin, Enantioselective catalysis with homochiral metal-organic frameworks, *Chem. Soc. Rev.*, 2009, **38**, 1248–1256.

19 A. H. Chughtai, N. Ahmad, H. A. Younus, A. Laypkov and F. Verpoort, Metal-organic frameworks: versatile heterogeneous catalysts for efficient catalytic organic transformations, *Chem. Soc. Rev.*, 2015, **44**, 6804–6849.

20 J. Yang, Y.-B. Zhang, Q. Liu, C. Trickett, E. Gutierrez-Puebla, M. Monge, H. Cong, A. Aldossary, H. Deng and O. Yaghi, Principles of Designing Extra-Large Pore Openings and Cages in Zeolitic Imidazolate Frameworks, *J. Am. Chem. Soc.*, 2017, **139**, 6448–6455.

21 W. Morris, J. Doonan, H. Furukawa, R. Banerjee and O. Yaghi, Crystals as Molecules: Postsynthesis Covalent Functionalization of Zeolitic Imidazolate Frameworks, *J. Am. Chem. Soc.*, 2008, **130**, 12626–12627.

22 L. Chai, Q. Huang, H. Cheng, X. Wang, L. Zhang, T.-T. Li, Y. Hu, J. Qian and S. Huang, Bottom-up preparation of hierarchically porous MOF-modified carbon sphere derivatives for efficient oxygen reduction, *Nanoscale*, 2020, **12**, 8785–8792.

23 L. Chai, L. Zhang, X. Wang, Z. Hu, Y. Xu, T.-T. Li, Y. Hu, J. Qian and S. Huang, Cube-shaped metal-nitrogen-carbon derived from metal-ammonia complex-impregnated metal-organic framework for highly efficient oxygen reduction reaction, *Carbon*, 2020, **158**, 719–727.

24 L. Chai, Z. Hu, X. Wang, L. Zhang, T.-T. Li, Y. Hu, J. Pan, J. Qian and S. Huang, Fe_7C_3 nanoparticles with in situ grown CNT on nitrogen doped hollow carbon cube with greatly enhanced conductivity and ORR performance for alkaline fuel cell, *Carbon*, 2021, **174**, 531–539.

25 F. Li, T. Qin, Y. Sun, R. Jiang, J. Yuan, X. Liu and A. P. O'Mullane, Preparation of a one-dimensional hierarchical MnO@CNT@Co-N/C ternary nanostructure as a high-performance bifunctional electrocatalyst for rechargeable Zn–air batteries, *J. Mater. Chem. A*, 2021, **9**, 22533–22543.

26 T. Liu, S. Feng, J. Huo, Q. Li, C. Xie and S. Wang, Crystalline-Water/Coordination Induced Formation of 3D Highly Porous Heteroatom-Doped Ultrathin Carbon Nanosheet Networks for Oxygen Reduction Reaction, *ChemCatChem*, 2018, **10**, 4562–4568.

27 Y. Guan, N. Li, Y. Li, L. Sun, L. Gao, Q. Zhang, C. He, J. Liu and X. Ren, Two dimensional ZIF-derived ultra-thin Cu-N/C

2566 | *Inorg. Chem. Front.*, 2022, **9**, 2557–2567

This journal is © the Partner Organisations 2022

nanosheets as high performance oxygen reduction electro-catalysts for high-performance Zn-air batteries, *Nanoscale*, 2020, **12**, 14259–14266.

28 R. Baker, D. P. Wilkinson and J. Zhang, Electrocatalytic activity and stability of substituted iron phthalocyanines towards oxygen reduction evaluated at different temperatures, *Electrochim. Acta*, 2008, **53**, 6906–6919.

29 H. Jia, Y. Yao, J. Zhao, Y. Gao, Z. Luo and P. Du, A novel two-dimensional nickel phthalocyanine-based metal-organic framework for highly efficient water oxidation catalysis, *J. Mater. Chem. A*, 2018, **6**, 1188–1195.

30 X. Zhang, R. Lin, X. Meng, W. Li, F. Chen and J. Hou, Iron Phthalocyanine/Two-Dimensional Metal-Organic Framework Composite Nanosheets for Enhanced Alkaline Hydrogen Evolution, *Inorg. Chem.*, 2021, **60**, 9987–9995.

31 Z. Zeng, X. Fang, W. Miao, Y. Liu, T. Maiyalagan and S. Mao, Electrochemically Sensing of Trichloroacetic Acid with Iron(II) Phthalocyanine and Zn-Based Metal Organic Framework Nanocomposites, *ACS Sens.*, 2019, **4**, 1934–1941.

32 A. Morozan, M. T. Sougrati, V. Goellner, D. Jones, L. Stievano and F. Jaouen, Effect of Furfuryl Alcohol on Metal Organic Framework-based Fe/N/C Electrocatalysts for Polymer Electrolyte Membrane Fuel Cells, *Electrochim. Acta*, 2014, **119**, 192–205.

33 G. Song, Z. Wang, L. Wang, G. Li, M. Huang and F. Yin, Preparation of MOF(Fe) and its catalytic activity for oxygen reduction reaction in an alkaline electrolyte, *Chin. J. Catal.*, 2014, **35**, 185–195.

34 J.-W. Huang, Y.-B. Chen, J.-M. Yang, H.-B. Zhu and H. Yang, Boosting the oxygen reduction performance of MOF-5-derived Fe-N-C electrocatalysts via a dual strategy of cation-exchange and guest-encapsulation, *Electrochim. Acta*, 2021, **366**, 137408.

35 W. Yang, Y. Zhang, X. Liu, L. Chen and J. Jia, In situ formed Fe-N doped metal organic framework@carbon nanotubes/graphene hybrids for a rechargeable Zn-air battery, *Chem. Commun.*, 2017, **53**, 12934–12937.

36 J. Zhou, P. N. Duchesne, Y. Hu, J. Wang, P. Zhang, Y. Li, T. Regier and H. Dai, Fe-N bonding in a carbon nanotube-graphene complex for oxygen reduction: an XAS study, *Phys. Chem. Chem. Phys.*, 2014, **16**, 15787–15791.

37 J. A. Varnell, E. M. Tse, C. Schulz, T. Fister, R. Haasch, J. Timoshenko, A. Frenkel and A. Gewirth, Identification of carbon-encapsulated iron nanoparticles as active species in non-precious metal oxygen reduction catalysts, *Nat. Commun.*, 2016, **7**, 12582.

38 X. C. Huang, Y. Y. Lin, J. P. Zhang and X. M. Chen, Ligand-directed strategy for zeolite-type metal-organic frameworks: zinc(II) imidazolates with unusual zeolitic topologies, *Angew. Chem., Int. Ed.*, 2006, **45**, 1557–1559.

39 Q. Yang, Q. Xu and H. L. Jiang, Metal-organic frameworks meet metal nanoparticles: synergistic effect for enhanced catalysis, *Chem. Soc. Rev.*, 2017, **46**, 4774–4808.

40 Y. Guo, A. Dong, Q. Huang, Q. Li, Y. Hu, J. Qian and S. Huang, Hierarchical N-doped CNTs grafted onto MOF-derived porous carbon nanomaterials for efficient oxygen reduction, *J. Colloid Interface Sci.*, 2020, **606**, 1833–1841.

41 Q. Huang, Y. Guo, X. Wang, L. Chai, J. Ding, L. Zhong, T.-T. Li, Y. Hu, J. Qian and S. Huang, In-MOF-derived ultra-thin heteroatom-doped carbon nanosheets for improving oxygen reduction, *Nanoscale*, 2020, **12**, 10019–10025.

42 H. Xu, S. Xi, J. Li, S. Liu, P. Lyu, W. Yu, T. Sun, D.-C. Qi, Q. He, H. Xiao, M. Lin, J. Wu, J. Zhang and J. Lu, Chemical design and synthesis of superior single-atom electrocatalysts via in situ polymerization, *J. Mater. Chem. A*, 2020, **8**, 17683–17690.

43 J. P. McClure, O. Borodin, M. Olguin, D. Chu and P. S. Fedkiw, Sensitivity of Density Functional Theory Methodology for Oxygen Reduction Reaction Predictions on Fe-N$_4$-Containing Graphitic Clusters, *J. Phys. Chem. C*, 2016, **120**, 28545–28562.

This journal is © the Partner Organisations 2022

Inorg. Chem. Front., 2022, **9**, 2557–2567 | **2567**